Hydrogen Storage Properties of the Ti18V24Nb23Cr33Al2 Multicomponent Alloy Using Ti6V4Al Alloy Scraps as Feedstock Material

Mariana de Brito Ferraz, Claudia Zlotea, Walter José Botta, Guilherme Zepon

Hydrogen storage properties of the $Ti_{18}V_{24}Nb_{23}Cr_{33}Al_2$ multicomponent alloy using Ti6V4Al alloy scraps as feedstock material

Mariana de Brito Ferraz[a], Claudia Zlotea[b], Walter José Botta[a,c], Guilherme Zepon[a,c*]

[a] Federal University of São Carlos, Graduate Program in Materials Science and Engineering (PPGCEM/UFSCar) - Rodovia Washington Luiz, Km 235, São Carlos, 13565-905, São Paulo, Brazil

[b] Institut de Chimie et des Matériaux de Paris-Est, CNRS UMR 7182, 2-8, Rue Henri Dunant, Thiais, France

[c] Federal University of São Carlos, Department of Materials Engineering (DEMa/UFSCar) - Rodovia Washington Luiz, Km 235, São Carlos,13565-905, São Paulo, Brazil

* Email: zepon@ufscar.br

ABSTRACT

Hydrogen storage in metal hydrides has been extensively studied due to their capacity to reversibly absorb hydrogen under relatively low pressures. Multicomponent alloys, especially those of the Ti-V-Nb-Cr system, have garnered significant attention because of the possibility of fine tuning the hydrogen storage properties by compositional control. However, most of the investigations on multicomponent alloys rely on high-purity elements as feedstock material, which can have a substantial environmental impact due to the energy-intensive processes required to achieve such purity levels. In this work, we propose an alternative approach by utilizing Ti6Al4V alloy (ASTM F136) scraps from the biomedical industry as feedstock material to produce $Ti_{18}Nb_{23}V_{24}Cr_{33}Al_2$. The alloy was synthesized using an arc-melting process, combining Ti6Al4V scraps with other pure elements. Structural analysis using X-ray diffraction (XRD) and Scanning Electron Microscopy (SEM) revealed the formation of a microstructure composed predominantly by a body-centered cubic (BCC) solid solution with a small micro segregation providing additional microstructural insights. The $Ti_{18}Nb_{23}V_{24}Cr_{33}Al_2$ alloy exhibited a hydrogen storage capacity of 2.75 wt.% H_2 with room temperature reversibility, presenting hydrogen storage properties comparable to the $(TiVNb)_{65}Cr_{35}$ alloy produced only from high-purity elements.

Keywords: hydrogen storage, metal hydride, bcc alloy, multicomponent alloy, Ti6Al4V alloy scraps.

Synopsis

This study presents a sustainable approach to producing $Ti_{18}Nb_{23}V_{24}Cr_{33}Al_2$ alloy from Ti6Al4V machine chips, achieving efficient hydrogen storage with reduced environmental impact.

Introduction

Fossil fuels have been a highly efficient energy source since the Industrial Revolution. However, in the 21st century, it has become clear that relying on them is unsustainable due to their harmful emissions and contribution to climate change gases (1). Hydrogen stands out as a sustainable alternative to store energy derived from clean and renewable sources, offering high energy content per unit of mass (2). Despite its potential, challenges such as safe storage and transportation hinder the expansion of the hydrogen economy. Efficient storage is vital to harness hydrogen's energy wherever and whenever needed. Hydrogen naturally has low volumetric and high gravimetric energy density (3). The main hydrogen storage methods include compressed gas, liquefied hydrogen, cryo-compressed, physical adsorption, complex hydrides, liquid organic hydrides, and metal hydrides (4). Notably, metal hydrides can achieve a volumetric density several times greater than compressed methods, storing large amounts of hydrogen in small spaces.

Recent studies have focused on multicomponent alloys due to their extensive compositional range, which allows the tuning of the hydrogen storage properties by composition control (5–13, 33-36). In 2019, Nygård et al. (13) investigated the TiVNb*M* (*M* = Cr, Zr, Mo, Hf, Ta) systems focusing on the relationship between valence-electron concentration (VEC) and the stability of high-entropy or multicomponent hydride alloys. The alloys synthesized via arc melting exhibited single body-centered cubic (BCC) phases and formed face-centered cubic (FCC) hydrides when the VEC was ≤ 5. Specifically, the TiVNbCr alloy with VEC = 5 was identified as a promising material for hydrogen storage because it presented a reversible hydrogen capacity of 1.96 wt.% at room temperature (RT) with absorption at 23 bar and desorption under dynamic vacuum, without requiring any activation procedure. Silva et al. (10) studied the $(TiVNb)_{85}Cr_{15}$ multicomponent produced by using arc melting, which also exhibits a single BCC phase structure in the as-cast condition. This alloy rapidly absorbs hydrogen under 20 bar of H_2 at RT by first forming a BCC monohydride (0.83 H/M and 1.33 wt% of H_2) and secondly forming an FCC hydride with 1.6 H/M and 2.54 wt.% of H_2. However, hydrogen capacity decreased during cycling due to the incomplete transformation from the BCC monohydride to the FCC dihydride.

Strozi et al. (8) investigated the $(TiVNb)_{100-x}Cr_x$ alloys with x = 15, 25, and 35 at. % Cr. These alloys were synthesized via arc melting and, as anticipated from thermodynamic calculations using the CALPHAD method, solidified as a major BCC solid solution. Under 20 bar of pressure, these alloys absorbed approximately 3 wt.% of hydrogen (~2 H/M) in the first absorption at RT without requiring activation procedure. The study concluded that Cr can effectively increase the equilibrium pressure without reducing the hydrogen capacity. Strozi et al. (14) continued their investigation into this system, focusing on $(TiVNb)_{100-x}Cr_x$ alloys (x = 30, 35, and 40). They employed the CALPHAD method for thermodynamic analysis and synthesized the alloys via arc melting. The alloys contain 30 %at. and 35 %at. Cr exhibited a stable BCC phase. In contrast, the $(TiVNb)_{60}Cr_{40}$ multicomponent alloy formed a major C15 Laves-type phase. The BCC phase alloys absorbed a substantial amount of hydrogen, forming FCC hydrides, whereas

the C15 alloy absorbed only 0.95 wt.%, with the lower capacity attributed to this phase. It was reported that increasing the Cr content beyond 35 at.% leads to the formation of a high fraction of the C15-type Laves phase, significantly reducing hydrogen storage capacity. In contrast, maintaining the Cr content at up to 35 at.% allows room-temperature absorption/desorption reversibility, reaching, approximately, 1 H/M of reversible capacity.

So far, most of the studies on multicomponent alloys for hydrogen storage, including those of the Ti-V-Nb-Cr system, employ the arc-melting process as production route using high-purity metals as feedstock material to achieve the alloy composition (14–19). There are different mandatory processes to achieve a high-purity metal, such as ore mining and concentration, smelting or separation, and refining (20). Over the stages, the metal concentration increases in the final product and by-products are separated. Refining a metal requires a huge amount of energy and precisely controlled melting stages are often necessary. These processes typically require heat and electricity, relying on fossil fuels (21).

For instance, one of the primary methods for producing titanium sponges, one of the main elements used in multicomponent alloys for hydrogen storage, is the Kroll process. Gao et al. (22) investigated titanium sponge production's environmental and energy impacts via the Kroll process in China, one of the world's largest producers. Their findings revealed that the process consumes approximately 423 GJ per ton of titanium sponge produced (22), which is approximately 18 times more than the energy consumed to produce one ton of steel and iron (23), demonstrating that primary Ti production is very energy intensive. According to Zeng (24), recycling strategic metals significantly contributes to conserving materials and energy. However, the rising demand for metals, driven by population growth and improved living standards, has increased recycling costs, undermining its contribution to sustainability. Therefore, reusing material waste from various processes is a viable option that offers significant environmental benefits, mainly when it replaces energy intensive metals such as primary Ti.

Some authors have already explored different strategies to use scrap materials to produce hydrogen storage alloys, such as Mg- and TiFe-based materials. These studies have demonstrated promising hydrogen storage properties and a potential contribution to reducing material costs (30-32). Following the same strategy and aiming at enhancing environmental sustainability in the production route of multicomponent alloys for hydrogen storage, this work investigates the hydrogen storage properties of the $(TiVNb)_{65}Cr_{35}$-based alloy produced using Ti6Al4V alloy (ASTM F136) scraps from the biomedical industry as feedstock material. Biomedical devices such as screws and prostheses are typically manufactured by machining Ti6Al4V ingots or bars. In these cases, approximately 50 % in weight or more of machining chips can be produced as a by-product of the machining process, which are usually discarded or downcycled to less noble applications. In this work, the $Ti_{18}Nb_{23}V_{24}Cr_{33}Al_2$ was produced by arc-melting using Ti6Al4V machining chips as feedstock material. This composition was based on the $(TiVNb)_{65}Cr_{35}$ alloy reported by Strozi et al. (14) due to its room-temperature hydrogen absorption/desorption reversibility. However, because of the presence of Al and V in the Ti6Al4V alloy, the final alloy composition includes 2 at. % of Al, accompanied by a reduction in the Ti content. The alloy

microstructure and hydrogen storage properties were compared with those presented by the pristine $(TiVNb)_{65}Cr_{35}$ alloy produced only from high-purity elements as reported by Strozi et al. (14).

Materials and methods

The $Ti_{18}Nb_{23}V_{24}Cr_{33}Al_2$ alloy was produced using Ti6Al4V alloy scraps (machining chips) provided by a Brazilian biomedical company. To remove the remaining oil-based machining lubricant fluid from the machining chips, a cleaning procedure using water and detergent in an ultrasound cleaner was carried out. The machining chips were immersed in water and detergent and left in the ultrasonic bath for about 15 minutes. This process was repeated with fresh water and detergent a few times until the surfaces appeared visually clean.

High-purity (>99.5%) chromium, niobium, and vanadium were used as feedstock material to achieve the desired chemical composition.

The feedstock materials were melted using an arc-melting Edmund Bühler Mini Arc Melter MAM-1 under an argon atmosphere. Before melting the alloys, a titanium getter was melted to reduce the oxygen concentration in the melting chamber. The alloy was remelted seven times to ensure chemical homogeneity in the bulk and was used as-cast without further annealing at high temperature.

Structural characterization of the Til6Al4V machining chips as well as the $Ti_{18}Nb_{23}V_{24}Cr_{33}Al_2$ alloy was conducted using X-ray diffraction (XRD) using a Bruker D8 Advance Eco diffractometer with Kα-Cu radiation. The XRD data was treated by Rietveld refinement using the GSAS II software (25). Additionally, scanning electron microscopy (SEM) using TESCAN MIRA FEG microscope was employed to analyze both the machining chips and the $Ti_{18}Nb_{23}V_{24}Cr_{33}Al_2$ alloy. Chemical microanalysis was carried out via energy-dispersive X-ray spectroscopy (EDS) using a Bruker Nano XFlash 6|30 EDS detector coupled to the SEM. For SEM analyses, part of the as-cast ingot of the $Ti_{18}Nb_{23}V_{24}Cr_{33}Al_2$ alloy was embedded in resin and subjected to grinding with sandpaper of varying granulometry, transitioning to a finer grit once the surface was uniformly oriented in a single direction. Upon reaching the finest grit (#1200), the sample was polished using 1 micron alumina suspension. The sample was cleaned with isopropyl alcohol, dried, and attached to an aluminum stub. To ensure proper electric contact, silver paint was applied between the sample and the stub.

The oxygen and nitrogen contents in the Ti6Al4V scraps were determined by infrared absorption and thermal conductivity detection using the LECO ONH-836 analyzer.

The hydrogen storage properties of the $Ti_{18}Nb_{23}V_{24}Cr_{33}Al_2$ were evaluated by volumetric techniques in a custom-built Sievert-type apparatus. The absorption kinetics were measured with and without the activation procedure. The activation procedure consisted of heating the sample from room temperature up to 400°C, maintaining it at 400°C under dynamic vacuum for 12 hours, and cooling it down to room temperature.

Absorption and desorption Pressure-Composition-Isotherms (PCIs) measurements at 25, 45, 60, and 75°C were conducted on activated samples after one complete absorption/desorption cycle.

Absorption/desorption cycling measurements were carried out at room temperature (25°C) by applying 75 bar of H_2 pressure for absorption and desorption under a dynamic vacuum for 30 minutes.

Results and discussion

Structural characterization of the Ti scraps

Figure 1 (a) presents a picture of the Ti6Al4V alloy machining chips used as feedstock material in this work after the cleaning procedure. The size of the chips varies from very small pieces, smaller than 2 mm up to 10 mm-long curly segments as indicated by the red arrow. Figure 1 (b) shows a secondary electron (SE) SEM image illustrating the morphology of the machining chips, which have a rough surface on one side and a smooth surface on the other. Figure 1 (c) shows the machining chips' XRD pattern, indicating that only hexagonal closed-packed (HCP) α-Ti is present. Although the Ti-6Al-4V is typically employed with an α+β microstructure, the machining chips were subjected to severe deformation and thermal cycle processes during cutting, which might alter their microstructure.

Table 1 presents the chemical composition of the Ti6Al4V alloy machining chips. A difference can be observed between the ASTM F136 standard composition (26) and the actual composition of the scraps. The Al and V content of the scraps is relatively lower when compared to minimum content allowed by the ASTM 136 standard. In addition, a higher Fe content if compared with the maximum content allowed is present. The Fe contamination is likely coming from the machining tools. One can observe that the oxygen content is just slightly above the maximum content allowed by the ASTM F136. The increase of O content is probably related to the surface oxidation of the machining chips during process. The N content is below the maximum content determined by the ASTM F136 standard. C and H contents were not possible to be measured.

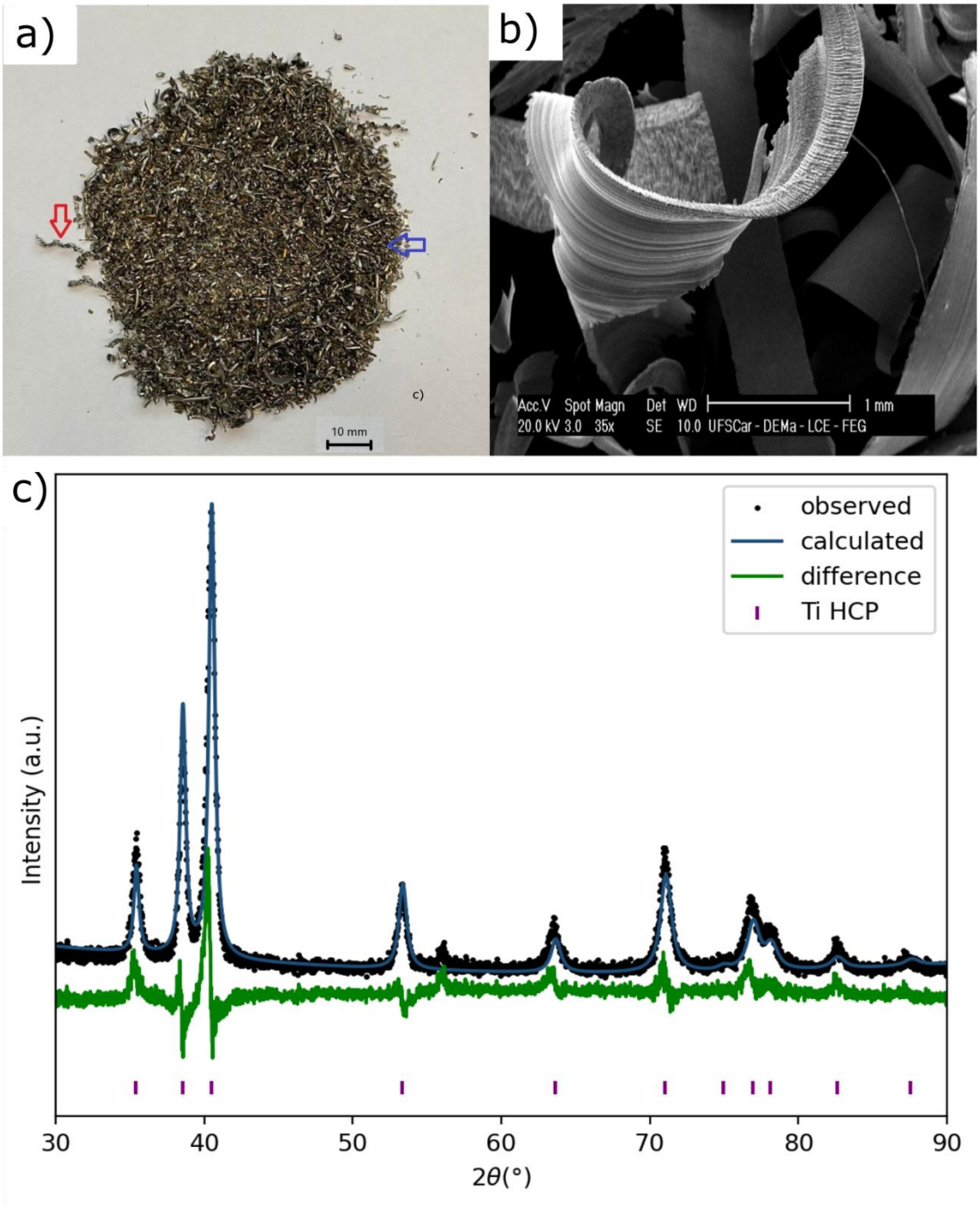

Figure 1: (a) Picture of the Ti6Al4V alloy machining chips used as feedstock material. (b) SE-SEM image and (c) XRD pattern and its respective Rietveld refinement results of the Ti6Al4V alloy machining chips. The lattice parameters of Ti hexagonal structure are a = 2.930(8) Å and c = 4.671(6) Å. Additionally, an unindexed peak at 56°, attributed to an artefact from XRD apparatus, is observed.

Table 1: Chemical composition of the Ti6Al4V alloy scraps. Ti, Al, V, and Fe contents were measured by EDS, O, and N using a LECO ONH-836 analyzer.

Elements	**Ti6Al4V scraps**	**F136 Standard** (26)
	%wt. - EDS	*%wt.*
Ti	90.3 ± 0.5	*90.75-88.75*
Al	5.7 ± 0.2	5.5-6.5
V	2.2 ± 0.2	3.5-4.5
Fe	1.8 ± 0.5	0.25 *max*.
	% wt. - LECO	
O	0.156	0.13 *max*
N	0.00256	0.05 *max*
C	-	0.08 *max*
H	-	0.12 *max*

Structural characterization of the as-cast $Ti_{18}Nb_{23}V_{24}Cr_{33}Al_2$ alloy

Figure 2 presents XRD pattern with the respective Rietveld refinement results for the as-cast $Ti_{18}Nb_{23}V_{24}Cr_{33}Al_2$ alloy produced using the Ti6Al4V alloy machining chips as feedstock material. The alloy presents a major BCC phase with a lattice parameter of a^{BCC} = 3.099(3) Å. In addition, the alloy presents a small fraction (2.3 wt.%) of a C15-type Laves phase with a lattice parameter of a^{C15} = 7.044(9) Å. These results are very similar to the results reported by Strozi et al. (14) for the $(TiVNb)_{65}Cr_{35}$ alloy produced using only high-purity elements as feedstock material.

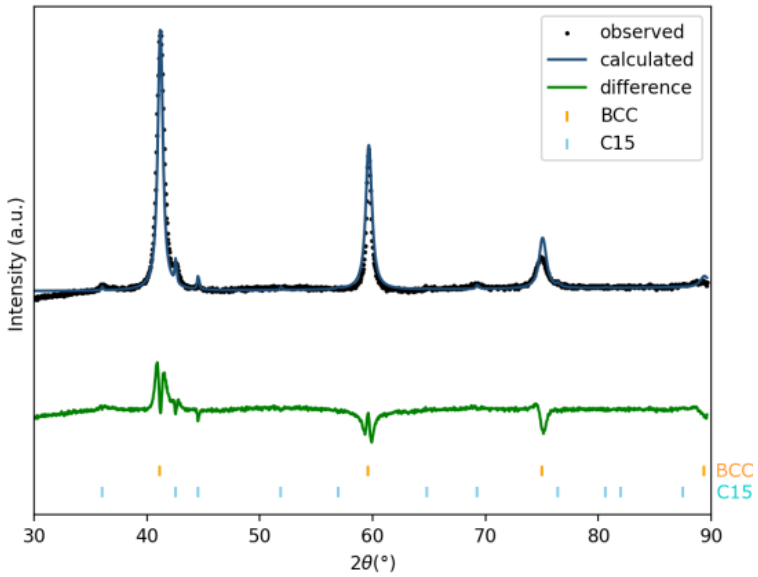

Figure 2: XRD pattern and its respective Rietveld refinement results of the as-cast $Ti_{18}Nb_{23}V_{24}Cr_{33}Al_2$ alloy produced using the Ti6Al4V alloy machining chips as feedstock material. a^{BCC} = 3.099(3) Å and a^{C15} = 7.045(9) Å.

Figure 3 presents backscattered electron (BSE) SEM images revealing that the as-cast $Ti_{18}Nb_{23}V_{24}Cr_{33}Al_2$ alloy exhibits a dendritic microstructure (brighter region), as shown in Figure 3(a), and a small fraction of a secondary phase at the interdendritic and grain boundary regions (darker region), as seen in Figure 3(b). The dendritic phase is the BCC solid solution, while the secondary phase at the interdendritic and grain boundary regions corresponds to the C15-type Laves phase. As shown in the EDS map presented in Figure 4, the BCC phase of the dendritic regions is enriched with Nb and V. In contrast, the C15-type Laves phase is richer in Ti and Cr, associated with the TiCr2 C15-type Laves phase. Table 2 shows the chemical composition of the as-cast $Ti_{18}Nb_{23}V_{24}Cr_{33}Al_2$ alloy. One can see that the overall chemical composition is very close to the nominal one. The chemical composition of the dendritic and interdendritic regions can also be observed in Table 2, confirmed that the interdendritic regions are slightly richer in Ti and Cr, while the dendritic region is richer in Nb and V. These results indicate the presence of a small chemical composition gradient from the dendritic to the interdendritic region. EDS mapping and quantitative EDS analyses indicate that the Al content is relatively well distributed in both dendritic and interdendritic regions.

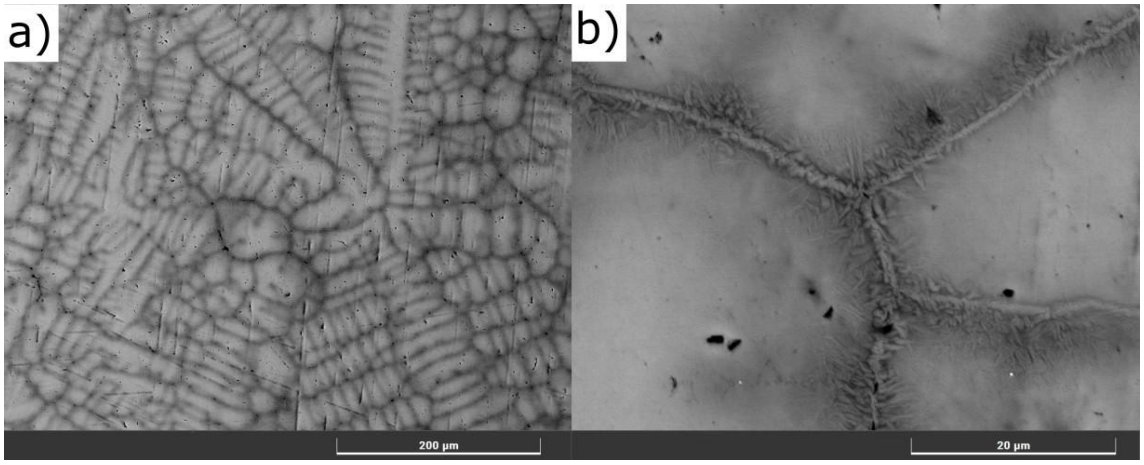

Figure 3: BSE-SEM images of the as-cast $Ti_{18}Nb_{23}V_{24}Cr_{33}Al_2$ alloy produced with Ti6Al4V alloy scraps as feedstock material. (a) Dendritic microstructure; (b) Grain boundary decorated with a secondary phase (C15-type Laves phase).

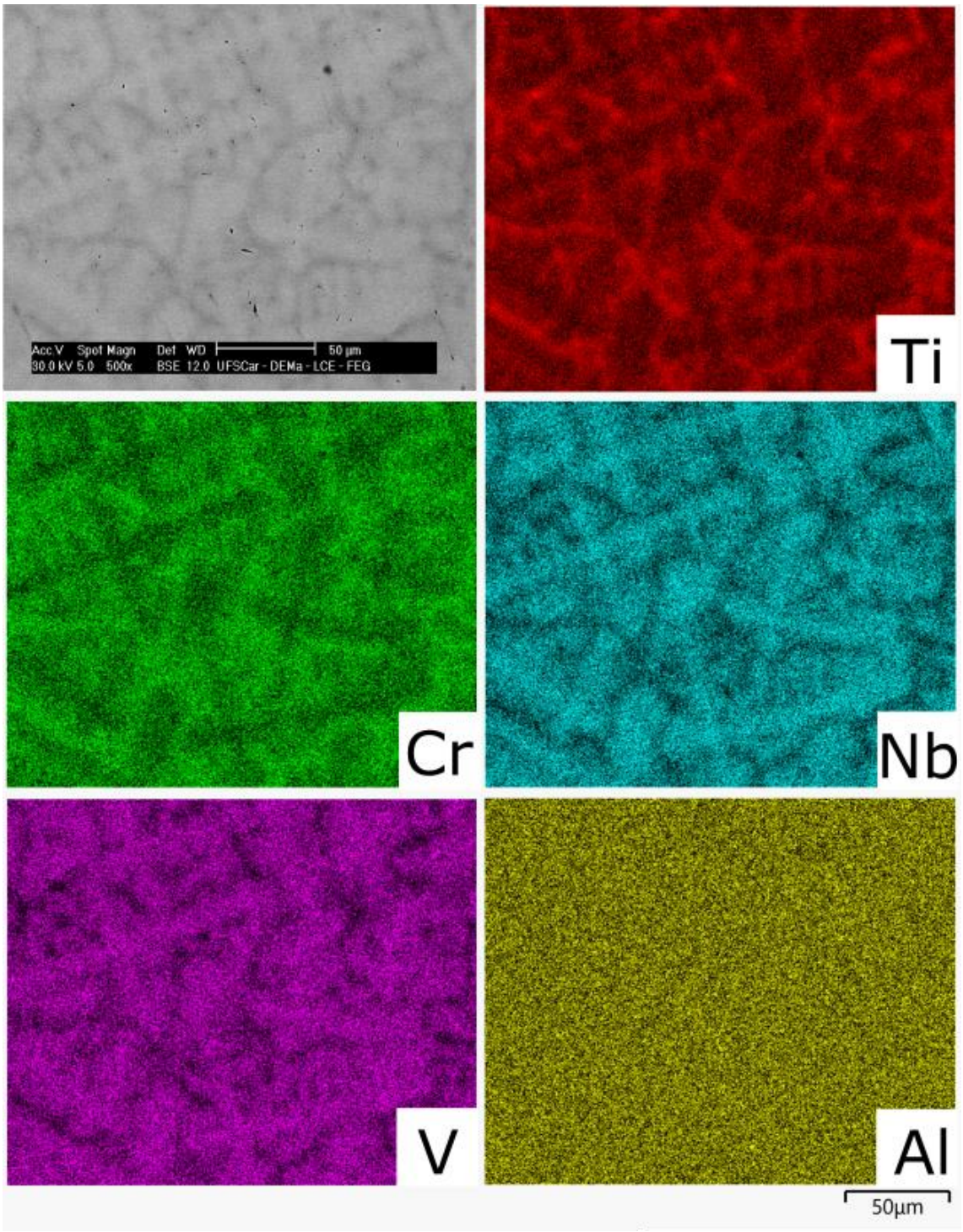

Figure 4: EDS maps of the as-cast $Ti_{18}Nb_{23}V_{24}Cr_{33}Al_2$ alloy produced with Ti6Al4V alloy scraps as feedstock material.

Table 2: Chemical composition measured by EDS of the as-cast $Ti_{18}Nb_{23}V_{24}Cr_{33}Al_2$ alloy produced with Ti 6Al4V alloy scraps as feedstock material.

Elements	Overall (at. %)	Dendrites (at. %)	Interdentrites regions (at. %)
Ti	18.4 ± 0.1	16.7 ± 0.2	20.3 ± 0.7
Nb	22.7 ± 0.3	24.6 ± 0.1	21.1 ± 0.4
Cr	32.9 ± 0.1	30.8 ± 0.1	34.9 ± 0.4
V	23.8 ± 0.1	26.0 ± 0.1	21.7 ± 0.7
Al	2.2 ± 0.5	1.8 ± 0.1	2.0 ± 0.1

Hydrogen storage properties of the as-cast $Ti_{18}Nb_{23}V_{24}Cr_{33}Al_2$ alloy

Figure 5 presents the results of room-temperature hydrogen absorption kinetics for the as-cast $Ti_{18}Nb_{23}V_{24}Cr_{33}Al_2$ alloy without and with the activation procedure. The $Ti_{18}Nb_{23}V_{24}Cr_{33}Al_2$ alloy can absorb hydrogen at room temperature without any activation procedure. The kinetic curve under 75 bar presents an incubation time of approximately seven minutes, followed by a relatively fast H absorption, reaching 1.8 %wt. of H in 15 minutes. The thermal activation procedure (400°C under dynamic vacuum for 12 hours) increases the H absorption kinetics of the alloy, eliminating the incubation period and reaching the maximum capacity of approximately 2.7 %wt. of H in less than three minutes. This maximum hydrogen storage capacity is very close to the one observed for the $(TiVNb)_{65}Cr_{35}$ produced using high purity elements reported in (14).

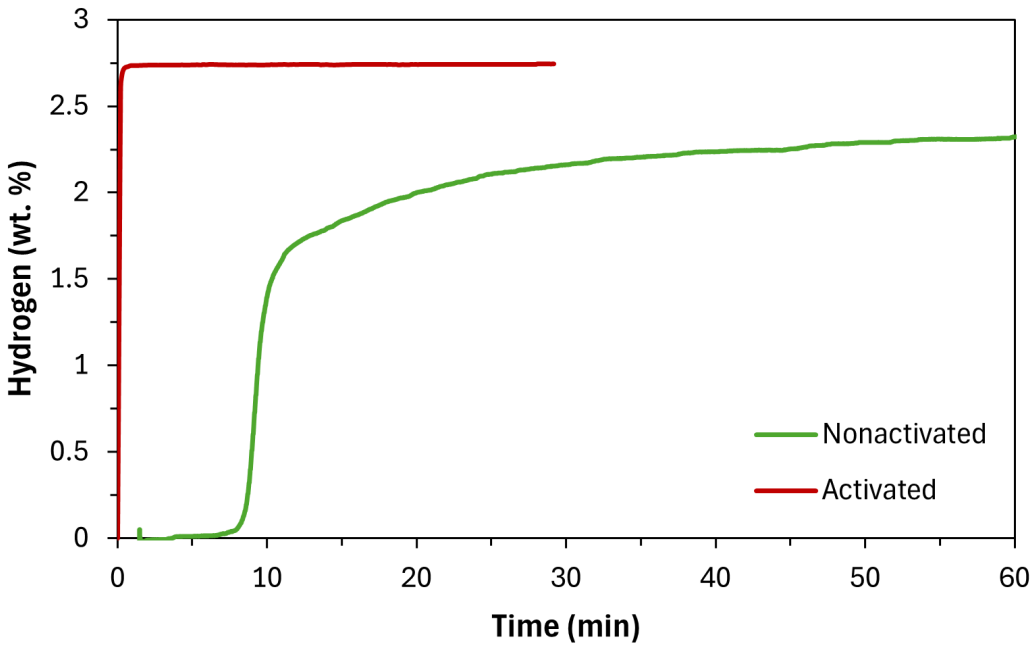

Figure 5: Room-temperature H absorption kinetic curves for the as-cast $Ti_{18}Nb_{23}V_{24}Cr_{33}Al_2$ alloy without and with activation treatment. Absorption pressure of 75 bar.

Figure 6 presents the Rietveld refinement analysis of the $Ti_{18}Nb_{23}V_{24}Cr_{33}Al_2$ alloy after H absorption, showing that an FCC hydride (CaF_2-type structure) was formed. The lattice parameter of the FCC hydride was a^{FCC} = 4.331(5) Å, which is also very close to the observed for the $(TiVNb)_{65}Cr_{35}$ produced using high-purity elements (14). In addition to the FCC hydride, an important fraction of an intermediate BCC hydride with lattice parameter of a^{BCC}= 3.201(1) Å could also be detected. It is well known that most of the BCC alloys absorb hydrogen in a multi-step process. First, the BCC absorbs hydrogen by interstitial solid solution. Then, a BCC (or BCT) intermediate hydride with H/M ranging from 0.5 H/M to 1.0 H/M is formed. Finally, an FCC hydride with ~2 H/M is formed (19). The detection of the intermediate BCC hydride in the XRD after the sample's removal from the hydrogen reactor suggests that the FCC hydride is relatively unstable. It may spontaneously desorb part of its hydrogen under ambient conditions, as noted by Strozi et al. (14).

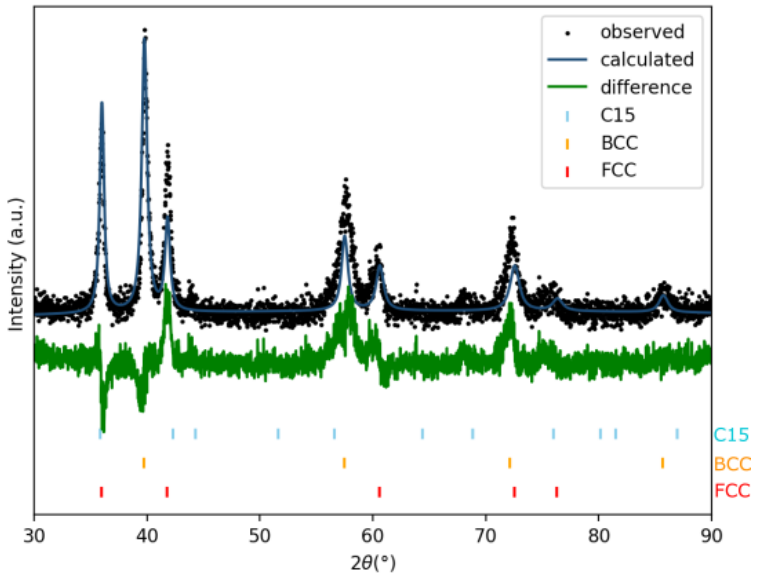

Figure 6: XRD pattern and corresponding Rietveld refinement results of the $Ti_{18}Nb_{23}V_{24}Cr_{33}Al_2$ alloy after hydrogen absorption, showing phase fractions of approximately 81.9 wt.% FCC, 15.8 wt.% BCC, and 2.3 wt.% C15.

Figure 7 (a) presents the Pressure-Composition-Isotherms (PCIs) curves measured under absorption and desorption for the $Ti_{18}Nb_{23}V_{24}Cr_{33}Al_2$ alloy at 75 °C, 60 °C, 45 °C, and 25 °C. Regardless of the temperature, one can see that the intermediate BCC hydride is formed at low pressures, with equilibrium plateau pressures below 10^{-1} bar, absorbing approximately 0.8 %wt. of H. The PCI curves present plateau pressures where the intermediate BCC hydride is in equilibrium with the FCC hydride. The plateau pressures are relatively sloped, which is common for as-cast BCC alloys with some chemical composition gradient (as observed in Figure 4 and Table 2) (27). At 25°C, the absorption plateau pressure is about 8 to 11 bar, while the desorption plateau is around 2 bar. The desorption plateau above 1 bar at 25 ºC confirms that the FCC hydride is indeed unstable under near-ambient conditions as reported by Strozi et al. (8), explaining the partial desorption when the alloy is exposed to ambient pressure and the presence

of the intermediate BCC hydride observed in the XRD pattern of Figure 6. One can also observe in Figure 7 (a) that as the temperature rises, the maximum hydrogen uptake measured in the PCI decreases. As the temperature rises, the equilibrium plateau pressure also increases. As the alloy presents slopped plateau pressures, the plateau is not completed at higher temperatures when 100 bar is applied, which is the maximum achievable pressure in the employed Sieverts apparatus. However, if a higher pressure was applied, maybe the same capacity observed at 25 ºC could be measured. The same behavior was reported for similar alloys in (8, 14).

Figure 7 (b) shows the Van't Hoff plot for the absorption and desorption plateau pressures versus the reciprocal temperature for the $Ti_{18}Nb_{23}V_{24}Cr_{33}Al_2$ alloy which were linearized to obtain both the plateau enthalpy and plateau entropy using the well-known Van't Hoff equation. Table 3 presents the comparison between the plateau enthalpies and entropies for the $Ti_{18}Nb_{23}V_{24}Cr_{33}Al_2$ alloy produced from Ti6Al4V scraps and the $(TiVNb)_{65}Cr_{35}$ alloy produced from high purity elements reported in (14). The plateau enthalpies for absorption/desorption are -32.5/+36.9 kJ/mol of H_2 and -39.0/+44.0 kJ/mol of H_2 for the $Ti_{18}Nb_{23}V_{24}Cr_{33}Al_2$ and $(TiVNb)_{65}Cr_{35}$ alloys, respectively. The lower absolute values for the plateau enthalpies confirm the lower stability of the FCC hydride of the $Ti_{18}Nb_{23}V_{24}Cr_{33}Al_2$ alloy compared with the $(TiVNb)_{65}Cr_{35}$ alloy. Such lower stability can be explained by the small Al content in the former alloy, which has been reported as a strong hydride destabilizer (24), and by its lower Ti content, which is a strong hydride stabilizer as reported in (28). In terms of plateau entropies, both alloys present similar values around -130 J/K. mol of H_2.

The lower stability of the FCC hydride for the $Ti_{18}Nb_{23}V_{24}Cr_{33}Al_2$ alloy can favor room-temperature absorption/desorption reversibility. Figure 8 presents the maximum H uptake for the $Ti_{18}Nb_{23}V_{24}Cr_{33}Al_2$ alloy during 20 absorption/cycles. The absorption measurements were carried out at room temperature and 75 bar of initial pressure. The desorption cycles were also carried out at room temperature by subjecting the sample to a dynamic vacuum for 15 minutes. In the first absorption cycle, a maximum H uptake of 2.7 wt.% of H was observed. In the second cycle, the maximum H uptake was 2.0 wt.% of H because the intermediate BCC hydride cannot be desorbed at room temperature even under dynamic vacuum. Over cycling, only a small reduction of the maximum H uptake is observed. It is worth noting that the absorption/desorption capacity does not decrease smoothly from the second to the 20th cycle due to small variation of the reservoir and sample holder temperature during the room-temperature cycling test. The cycling stability of the $Ti_{18}Nb_{23}V_{24}Cr_{33}Al_2$ produced from Ti6Al4V scraps is comparable to the $(TiVNb)_{65}Cr_{35}$ alloy produced from high-purity elements (14) as can be seen in Figure 8. It is worth mentioning that the absorption measurement for the $(TiVNb)_{65}Cr_{35}$ alloy was carried out at 15 bar and, therefore, these results cannot be straightforwardly compared to each other.

Table 3: Plateau enthalpies and entropies for the $Ti_{18}Nb_{23}V_{24}Cr_{33}Al_2$ alloy produced from Ti6Al4V scraps and the $(TiVNb)_{65}Cr_{35}$ alloy produced from high purity elements reported in (14) .

Alloy	ΔH_{abs} (kJ/mol of H_2)	ΔH_{des} (kJ/mol of H_2)	ΔS_{abs} (J/mol of H_2)	ΔS_{des} (J/mol of H_2)
$Ti_{18}Nb_{23}V_{24}Cr_{33}Al_2$	-32.5 ± 2.7	36.9 ± 5.3	-127.8 ± 8	127.8 ± 16
$(TiVNb)_{65}Cr_{35}$ (14)	-39.0	44.0	-134.0	137.0

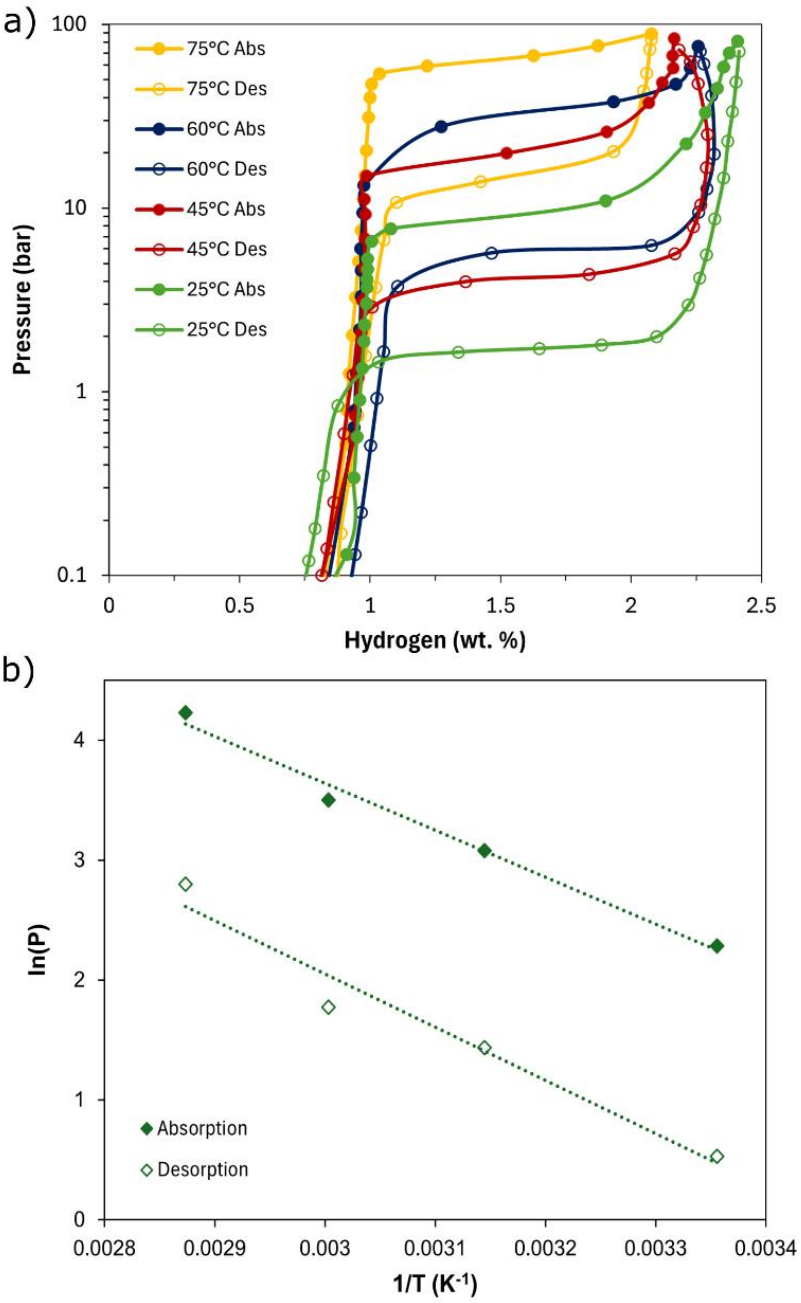

Figure 7: (a) Pressure-Composition-Isotherm (PCI) curves with filled circles representing absorption and empty circles representing desorption, respectively, and **(b)** Van't Hoff plot of the

absorption (filled circles) and desorption (empty circles) plateau pressures versus the reciprocal temperature for the $Ti_{18}Nb_{23}V_{24}Cr_{33}Al_2$ alloy produced with Ti6Al4V alloy scraps as feedstock material.

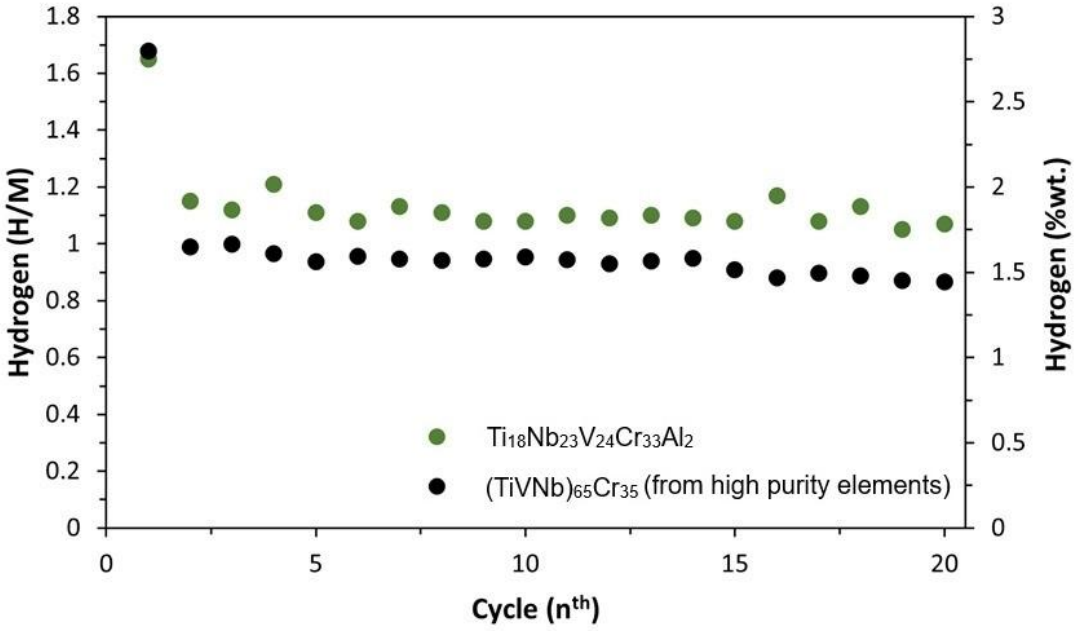

Figure 8: Comparison between the maximum H uptake during room-temperature absorption/desorption cycling for the $Ti_{18}Nb_{23}V_{24}Cr_{33}Al_2$ alloy produced from Ti6Al4V scraps and the $(TiVNb)_{65}Cr_{35}$ alloy produced from high purity elements reported in (14). Absorption pressure for the $Ti_{18}Nb_{23}V_{24}Cr_{33}Al_2$ alloy: 75 bar. Absorption pressure for the $(TiVNb)_{65}Cr_{35}$ alloy: 15 bar. Desorption at room temperature under dynamic vacuum for 15 minutes.

Considering that minimal effort was required to prepare the Ti6Al4V scraps used to produce the alloy, simply reusing these materials as feedstock material for a noble application such as a hydrogen storage media — repurposing them effectively — represents a significant contribution to sustainability. The hydrogen storage properties of the alloy synthesized from Ti6Al4V scraps as feedstock are highly promising, achieving a maximum capacity of 2.7 wt.% at room temperature, with hydrogen properties comparable to the $(TiVNb)_{65}Cr_{35}$ alloy produced from high-purity elements and others BCC multicomponent alloys that have been investigated for hydrogen storage applications [8,14,17,28,29]. Moreover, the incorporation of Al in the alloy composition decreased the stability of the FCC hydride formed, favoring the absorption/desorption reversibility at room temperature. The results suggest that repurposing Ti6Al4V scraps as feedstock for producing multicomponent alloys represents a promising first step toward utilizing recyclable materials in hydrogen storage applications.

4 Conclusion

This study aimed to replace high-purity Ti by Ti6Al4V scraps in producing the $(TiVNb)_{65}Cr_{35}$ alloy for hydrogen storage applications. The primary goal was to compare the microstructure and hydrogen storage properties of two alloys: the $(TiVNb)_{65}Cr_{35}$ alloy produced by Strozi et al. (18) using high-purity Ti and the $Ti_{18}Nb_{23}V_{24}Cr_{33}Al_2$ alloy produced using Ti6Al4V scrap as feedstock material. The findings revealed that both alloys shared the same primary phases, predominantly BCC, indicating that using Ti6Al4V scraps did not alter the phase structure compared to the alloy based on pure Ti. The equilibrium pressure was higher because of the Al presence and the decreased Ti content and the $Ti_{18}Nb_{23}V_{24}Cr_{33}Al_2$ alloy exhibited promising hydrogen storage properties, with a capacity of 2.7 wt.% at room temperature. The reduced stability of the FCC hydride in the $Ti_{18}Nb_{23}V_{24}Cr_{33}Al_2$ alloy, compared to the $(TiVNb)_{65}Cr_{35}$ alloy (14), is reflected in its lower absolute plateau enthalpy values. This behavior is primarily attributed to the reduced titanium content, a key stabilizer of hydrides, and the presence of 2 at. % aluminum, which acts as a potent destabilizer resulting in improving the equilibrium pressure. The recycled alloy demonstrated improved stability over the high-pure elements alloy (14), suggesting enhanced durability. Therefore, these results highlight the potential of using recycled Ti for sustainable hydrogen storage materials without compromising performance.

Acknowledgments

This work is financially supported in part by the Serrapilheira Institute (grant number Serra-1709-17362), in part by Brazilian National Council for Scientific and Technological Development – CNPq (grant numbers: 309467/2021-7 and 407906/2022-3), and in part by Coordenação de Aperfeiçoamento de Pessoal de Nível Superior - Brasil (CAPES) - Código Financeiro 001. The authors thank the Structural Characterization Laboratory (LCE) at the Federal University of São Carlos (UFSCar) for the electron microscopy and X-ray diffraction facilities.

References

(1) Hoel M, Kvemdokk S. Depletion of fossil fuels and the impacts of global warming. vol. 18. 1996.

(2) Durbin DJ, Malardier-Jugroot C. Review of hydrogen storage techniques for on board vehicle applications. Int J Hydrogen Energy 2013;38:14595–617. https://doi.org/10.1016/j.ijhydene.2013.07.058.

(3) Zhang F, Zhao P, Niu M, Maddy J. The survey of key technologies in hydrogen energy storage. Int J Hydrogen Energy 2016;41:14535–52. https://doi.org/10.1016/j.ijhydene.2016.05.293.

(4) Usman MR. Hydrogen storage methods: Review and current status. Renewable and Sustainable Energy Reviews 2022;167. https://doi.org/10.1016/j.rser.2022.112743.

(5) Zhang J, Li P, Huang G, Zhang W, Hu J, Xiao H, et al. metals Superior Hydrogen Sorption Kinetics of Ti 0.20 Zr 0.20 Hf 0.20 Nb 0.40 High-Entropy Alloy 2021. https://doi.org/10.3390/met.

(6) Karlsson D, Ek G, Cedervall J, Zlotea C, Møller KT, Hansen TC, et al. Structure and Hydrogenation Properties of a HfNbTiVZr High-Entropy Alloy. Inorg Chem 2018;57:2103–10. https://doi.org/10.1021/acs.inorgchem.7b03004.

(7) Andrade G, Silva BH, Zepon G, Floriano R. Hydrogen storage properties of Zr-based multicomponent alloys with C14-Laves phase structure derived from the Zr–Cr–Mn–Fe–Ni system. Int J Hydrogen Energy 2024;51:246–54. https://doi.org/10.1016/j.ijhydene.2023.11.111.

(8) Strozi RB, Leiva DR, Zepon G, Botta WJ, Huot J. Effects of the chromium content in (Tivnb)100−xcrx body-centered cubic high entropy alloys designed for hydrogen storage applications. Energies (Basel) 2021;14. https://doi.org/10.3390/en14113068.

(9) Ponsoni JB, Aranda V, Nascimento T da S, Strozi RB, Botta WJ, Zepon G. Design of multicomponent alloys with C14 laves phase structure for hydrogen storage assisted by computational thermodynamic. Acta Mater 2022;240. https://doi.org/10.1016/j.actamat.2022.118317.

(10) Silva BH, Zlotea C, Champion Y, Botta WJ, Zepon G. Design of TiVNb-(Cr, Ni or Co) multicomponent alloys with the same valence electron concentration for hydrogen storage. J Alloys Compd 2021;865. https://doi.org/10.1016/j.jallcom.2021.158767.

(11) Chanchetti LF, Hessel Silva B, Montero J, Zlotea C, Champion Y, Botta WJ, et al. Structural characterization and hydrogen storage properties of the Ti31V26Nb26Zr12M5 (M = Fe, Co, or Ni) multi-phase multicomponent alloys. Int J Hydrogen Energy 2023;48:2247–55. https://doi.org/10.1016/j.ijhydene.2022.10.060.

(12) Montero J, Ek G, Sahlberg M, Zlotea C. Improving the hydrogen cycling properties by Mg addition in Ti-V-Zr-Nb refractory high entropy alloy. Scr Mater 2021;194. https://doi.org/10.1016/j.scriptamat.2020.113699.

(13) Nygård MM, Ek G, Karlsson D, Sahlberg M, Sørby MH, Hauback BC. Hydrogen storage in high-entropy alloys with varying degree of local lattice strain. Int J Hydrogen Energy 2019;44:29140–9. https://doi.org/10.1016/j.ijhydene.2019.03.223.

(14) Strozi RB, Silva BH, Leiva DR, Zlotea C, Botta WJ, Zepon G. Tuning the hydrogen storage properties of Ti-V-Nb-Cr alloys by controlling the Cr/(TiVNb) ratio. J Alloys Compd 2023;932. https://doi.org/10.1016/j.jallcom.2022.167609.

(15) Ferreira T, Pineda-Romero N, Botta WJ, Zepon G, Zlotea C. Tuning the hydride stability of the TiVNb-based alloys by equimolar Cr/Al addition. Intermetallics (Barking) 2023;161. https://doi.org/10.1016/j.intermet.2023.107992.

(16) Pineda-Romero N, Perrière L, Elkaim E, Zlotea C. Advancing our understanding of the effect of Al/Mo substitution in the TiVNb alloy on the hydrogen storage properties. J Alloys Compd 2024;1005. https://doi.org/10.1016/j.jallcom.2024.176255.

(17) Mayer Dias GC, Silva BH, de Sousa Martins A, Felderhoff M, Botta WJ, Zepon G. Hydride Destabilization in the Ti-Nb-Cr System Through Nb/Ti Ratio Adjustment. ACS Appl Energy Mater 2024. https://doi.org/10.1021/acsaem.4c01167.

(18) Silva BH, Zlotea C, Champion Y, Botta WJ, Zepon G. Design of TiVNb-(Cr, Ni or Co) multicomponent alloys with the same valence electron concentration for hydrogen storage. J Alloys Compd 2021;865. https://doi.org/10.1016/j.jallcom.2021.158767.

(19) Silva BH, Zlotea C, Vaughan G, Champion Y, Botta WJ, Zepon G. Hydrogen absorption/desorption reactions of the (TiVNb)85Cr15 multicomponent alloy. J Alloys Compd 2022;901. https://doi.org/10.1016/j.jallcom.2022.163620.

(20) Gupta CK. Chemical metallurgy : principles and practice. Wiley-VCH; 2003.

(21) Nuss P, Eckelman MJ. Life cycle assessment of metals: A scientific synthesis. PLoS One 2014;9. https://doi.org/10.1371/journal.pone.0101298.

(22) Gao F, Nie Z, Yang D, Sun B, Liu Y, Gong X, et al. Environmental impacts analysis of titanium sponge production using Kroll process in China. J Clean Prod 2018;174:771–9. https://doi.org/10.1016/j.jclepro.2017.09.240.

(23) Hasanbeigi A, Price L, Chunxia Z, Aden N, Xiuping L, Fangqin S. Comparison of iron and steel production energy use and energy intensity in China and the U.S. J Clean Prod 2014;65:108–19. https://doi.org/10.1016/j.jclepro.2013.09.047.

(24) Zeng X. Win-Win: Anthropogenic circularity for metal criticality and carbon neutrality. Front Environ Sci Eng 2023;17. https://doi.org/10.1007/s11783-023-1623-2.

(25) Toby BH, Von Dreele RB. GSAS-II: The genesis of a modern open-source all purpose crystallography software package. J Appl Crystallogr 2013;46:544–9. https://doi.org/10.1107/S0021889813003531.

(26) Specification for Wrought Titanium-6Aluminum-4Vanadium ELI (Extra Low Interstitial) Alloy for Surgical Implant Applications (UNS R56401) 2013. https://doi.org/10.1520/F0136-13.

(27) Marques F, Balcerzak M, Winkelmann F, Zepon G, Felderhoff M. Review and outlook on high-entropy alloys for hydrogen storage. Energy Environ Sci 2021;14:5191–227. https://doi.org/10.1039/d1ee01543e.

(28) Strozi RB, Botta WJ, Zepon G. Effect of the interchangeability of Ti and Nb on the crystal structure and hydrogen storage properties of TixNb80-xAl10Cr10 (x = 30,

40, and 50) multicomponent alloys. Int J Hydrogen Energy 2024;91:185–95. https://doi.org/10.1016/j.ijhydene.2024.10.128.

(29) Li S, Hu H, Zhang X, Li C, Liu Y, Liu L, et al. Hydrogen storage in a novel BCC-structured TiCrW alloys. Chemical Engineering Journal 2025;503. https://doi.org/10.1016/j.cej.2024.157872.

(30) Pistidda C, Bergemann N, Wurr J, Rzeszutek A, Møller KT, Hansen BRS, et al. Hydrogen storage systems from waste Mg alloys. *J Power Sources*. 2014;270:554–63. https://doi.org/10.1016/j.jpowsour.2014.07.129.

(31) Hardian R, Pistidda C, Chaudhary A-L, Capurso G, Gizer G, Cao H, et al. Waste Mg-Al based alloys for hydrogen storage. *Int J Hydrogen Energy*. 2018;43(31):16738–48. https://doi.org/10.1016/j.ijhydene.2017.12.014.

(32) Shang Y, Liu S, Liang Z, Pyczak F, Lei Z, Heidenreich T, et al. Developing sustainable FeTi alloys for hydrogen storage by recycling. *Commun Mater*. 2022;3(101). https://doi.org/10.1038/s43246-022-00324-5.

(33) Zhai, Y.T., Li, Y.M., Liu, Z.C., Bolzoni, L., Kennedy, J., & Yang, F. (2025). Hydrogen ab/desorption behavior of the mechanical alloyed Ti–V–Cr–Mn–Fe HEAs with varying Mn/Cr ratio. *International Journal of Hydrogen Energy, 109*, 1008–1022. https://doi.org/10.1016/j.ijhydene.2025.02.139.

(34) Li, S., Hu, H., Zhang, X., Li, C., Liu, Y., Liu, L., & Chen, Q. (2025). Hydrogen storage in a novel BCC-structured TiCrW alloys. *Chemical Engineering Journal, 503*, 157872. https://doi.org/10.1016/j.cej.2024.157872.

(35) Zhai, Y.T., Li, Y.M., Wei, S.H., Tolj, I., Kennedy, J., & Yang, F. (2025). Progress in V-BCC based solid solution hydrogen storage alloys. *Journal of Energy Storage, 109*, 115103. https://doi.org/10.1016/j.est.2024.115103.

(36) Moussa, M., van Eijck, L., Huot, J., & Bobet, J. L. (2025). Structure analysis (XRD and Neutrons) and hydrogen storage properties of Hf1-xTixNbVZr BCC high entropy alloys. *Journal of Alloys and Compounds, 1010*, 177103. https://doi.org/10.1016/j.jallcom.2024.177103.

For Table of Contents Only